

Edge Effect on Crack Patterns in Thermally Sprayed Ceramic Splats

Lin Chen¹ · Guan-Jun Yang¹ · Cheng-Xin Li¹ · Chang-Jiu Li¹

Submitted: 22 June 2016 / in revised form: 27 September 2016 / Published online: 19 December 2016
© ASM International 2016

Abstract To explore the edge effect on intrasplat cracking of thermally sprayed ceramic splats, crack patterns of splats were experimentally observed and investigated through mechanical analysis. Both the polycrystalline splats and single-crystal splats showed obvious edge effects, i.e., preferential cracking orientation and differences in domain size between center fragments and edge fragments. In addition, substrate/interface delamination on the periphery was clearly observed for single-crystal splats. Mechanical analysis of edge effect was also carried out, and it was found that both singular normal stress in the substrate and huge peeling stress and shear stress at the interface were induced. Moreover, effective relief of tensile stress in splats is discussed. The good correspondence between experimental observations and mechanical analysis is elaborated. The edge effect can be used to tailor the pattern morphology and shed further light on coating structure design and optimization.

Keywords crack morphology · edge effect · preferential orientation · substrate stress · shear and peeling stress

Introduction

Because of the low thermal conductivity of lamellar coating structures, the thermal spray technique has become one of the most important approaches to depositing thermal barrier coatings for advanced gas turbines. Numerous interlamellar pores and intrasplat cracks are two essential characteristics of thermally sprayed ceramic coatings (Ref 1, 2). Although there have been many studies on intrasplat cracks, an in-depth understanding of the formation mechanism is not yet clear. To date, it is merely known that the existence of intrasplat cracks is usually due to stress relaxation during rapid cooling of ceramic splat (Ref 3–5). However, the final crack pattern is often considered to be disordered, because the segments are frequently regarded as having irregular morphology owing to the random appearance of intrasplat cracks (Ref 1, 6–8). Also, there is little information on how to effectively tailor the segment size. Where and how intrasplat cracks are initiated and propagated are also rarely reported.

In a previous study, intrasplat crack patterns were generally found to present a hierarchical structure, with four sides and six neighbors, arising from successive domain divisions owing to both sequential cracking and geometric constraints (Ref 9). The intrasplat crack patterns of a single-crystal splat presented a perfect hierarchy, whereas the hierarchy was somewhat different for polycrystalline splat crack patterns owing to intergranular cracking. However, there were some differences in the crack patterns at the periphery and in the center region in addition to the hierarchical characteristics, i.e., the intrasplat cracks preferred to propagate along the radial direction at the periphery. Furthermore, transverse delamination at/beneath the splat/substrate interface was often observed at the periphery. All of these factors, which are related to the free edges

✉ Guan-Jun Yang
ygj@mail.xjtu.edu.cn

¹ State Key Laboratory for Mechanical Behavior of Materials, School of Materials Science and Engineering, Xi'an Jiaotong University, Xi'an, Shaanxi 710049, People's Republic of China

of splats, complicate pattern morphologies. It is therefore necessary to identify this edge effect on intrasplat cracking.

In this study, the edge effect on intrasplat cracking was explored based on both experimental observation and mechanics analysis. The resulting understanding of both the hierarchical structure and the edge effect on intrasplat cracking will shed light on further coating structure design and optimization.

Experimental Procedure

Considering that thermal spray coatings are built up through successive deposition of lamellar splats, understanding of the single suffices to provide contributing direction. To comprehensively explore the edge effect in the present study, three kinds of powders, i.e., titania (TiO_2), 8 mol.% yttria-stabilized zirconia (YSZ), and lanthanum zirconate (LZ), were deposited on both single-crystal substrates and 304 stainless steel (304SS). The single-crystal substrates were square, with a width of 10 mm and a thickness of 500 μm . Additionally, both the TiO_2 and YSZ single-crystal substrates were of (001) plane with a well-polished surface finish ($R_a < 0.5 \text{ nm}$) and edge sides of $\langle 100 \rangle$ orientation. As shown in Fig. 1, the TiO_2 (Fig. 1a) fused-crushed powder had particle sizes ranging from 30 to 50 μm , whereas the YSZ (Fig. 1b) fused-crushed powder and LZ (Fig. 1c) agglomerate powder had particle sizes ranging from 5 to 25 μm , with a mean size of 17.8 μm . A commercial plasma spray system (GP-80, Jiujiang, China) was used to deposit splats under a plasma arc power of 44 kW and a spray distance of 80 mm. To achieve a disk-shaped splat by avoiding splat splashing, the substrate was preheated to 300 or 500 $^\circ\text{C}$ using a copper plate heater prior to splat deposition. The substrate surface temperature was monitored using a calibrated thermocouple. In addition, to avoid the calefaction of the plasma arc to the substrate, a shielding plate with several small holes was placed over the substrate. After splat deposition, the splat and substrate were cooled to room temperature in ambient atmosphere. The surface morphologies of the splats were examined using scanning electron microscopy (SEM, VEGA II-XMU, TESCAN, Czech Republic).

Edge Effect Based on Experimental Observation

Generally, the crack morphology of splats is influenced by many factors. Among them, grain boundary, which arises from rapid cooling, is a crucial one. To better understand the edge effect in this study, both polycrystalline and single-crystal splats were investigated.

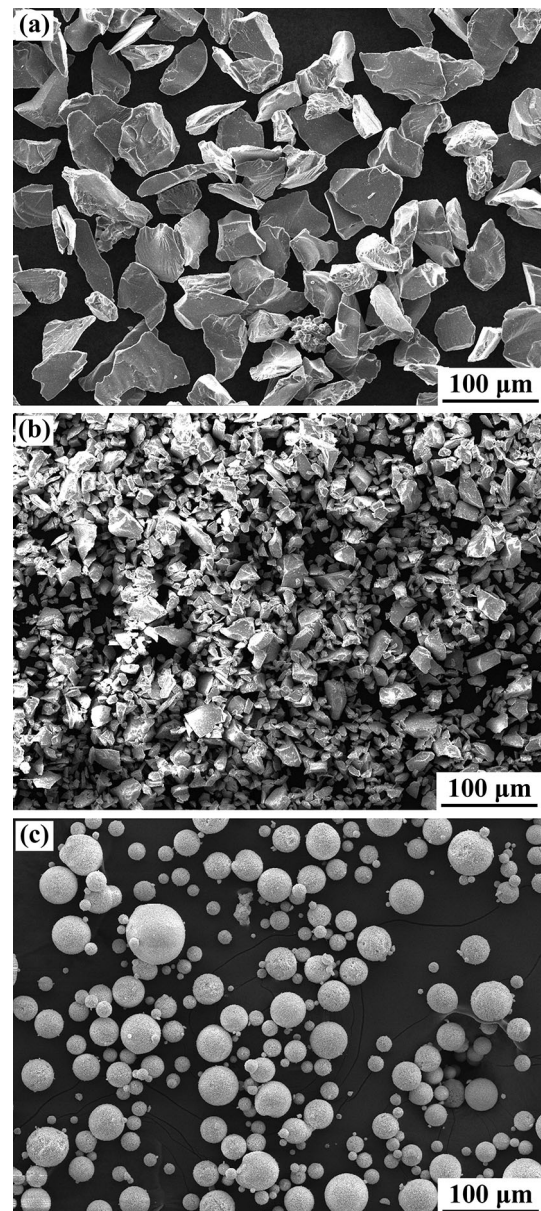


Fig. 1 Surface morphologies of (a) TiO_2 fused-crushed powder, (b) YSZ fused-crushed powder, and (c) LZ agglomerate powder

Edge Effect of Crack Patterns for Polycrystalline Splats

Firstly, crack morphologies of three kinds of polycrystalline splats were explored. All of the results revealed clear edge effects at the periphery.

Crack Patterns of Polycrystalline YSZ Splats

Figure 2 shows the overall surface morphology of YSZ splat deposited on a 304SS substrate. The crack pattern shown in Fig. 2(a) seems disordered because of zigzag crack paths which probably arose from the intergranular

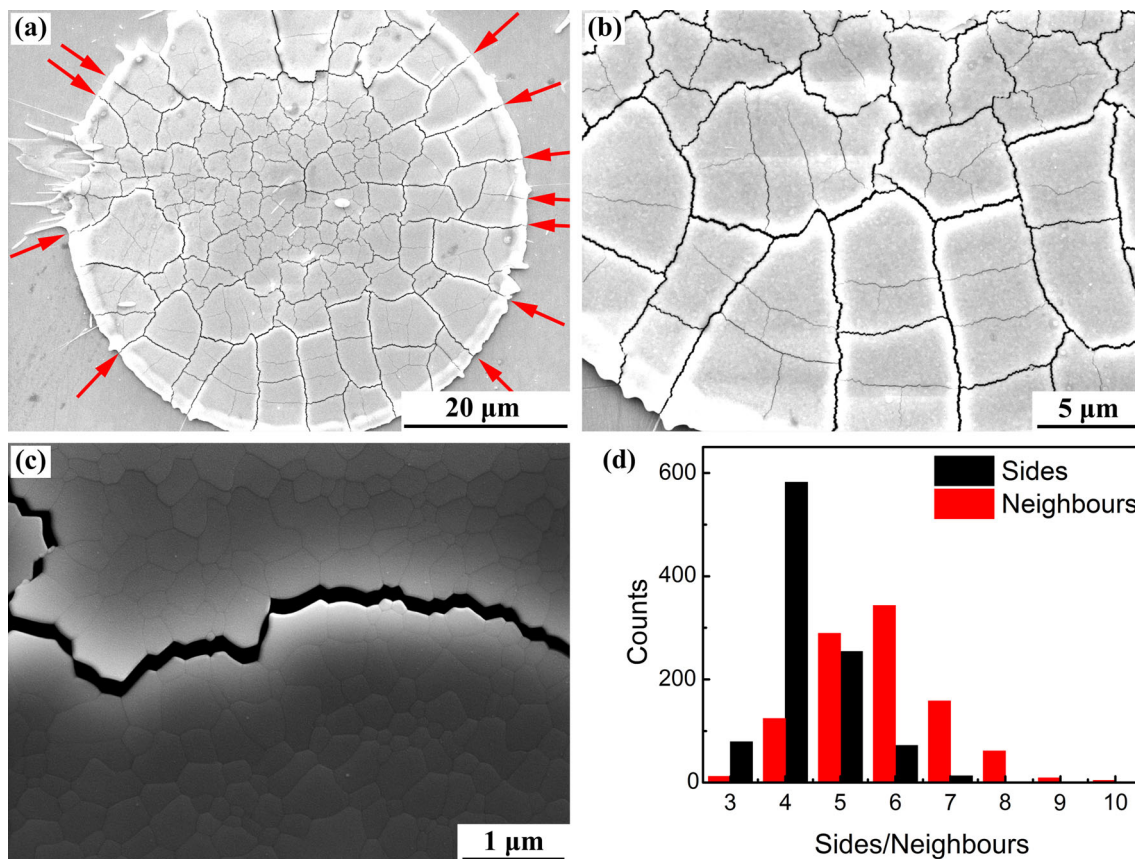


Fig. 2 Surface morphologies of YSZ splats on 304SS stainless steel substrate at (a) low magnification and (b, c) high magnification. The grains are clearly observed in (c). Statistics of both the number of sides and the number of neighbors for 1000 YSZ patterns are shown in (d)

cracking shown in Fig. 2(c). From the higher magnification image shown in Fig. 2(b), it is observed that the crack width is distributed across a wide area. However, cracks of different widths seem to be arranged somewhat regularly. Narrow cracks are generally located in the middle of wider cracks, and the domains surrounded by wide cracks are frequently divided into several smaller segments by narrower cracks. Based on the specific definition and distinction between topology and geometry reported in a previous study (Ref 9), statistics on both the number of sides and the number of neighbors were obtained, and the results are shown in Fig. 2(d). The average number of sides and number of neighbors of each pattern is 4.4 and 5.8, respectively. This clearly reveals that fragments of YSZ splats on 304SS roughly presented a hierarchical structure with four sides and six neighbors, which is an essential characteristic of a hierarchical morphology (Ref 9). However, it is noteworthy that, during this statistical process, the domains at the edge were not taken into account because the number of neighbors beyond the edge was not known.

The distinction of crack morphology between the center region and the periphery is clearly shown in Fig. 2(b). The cracks in the center region seem well disordered, whereas

the cracks on the periphery tend to show preferential cracking orientation. Figure 2(a) shows first-generation cracks preferentially oriented toward the splat center, as shown by the red arrows, and thus, they are perpendicular to the local edge. In addition, the second-generation cracks (narrow cracks in Fig. 2b) tend to be parallel to the splat edge, i.e., they are preferentially perpendicular to the first-generation cracks according to a previous study (Ref 9). Second, the domains that are divided by the intrasplat cracks are much larger than those in the center of the splat. To further prove the hierarchical morphology of the periphery, the average number of sides and number of neighbors of the edge fragments were also counted and found to be 4.1 and 4.8, respectively. Taking one free edge of each edge fragment into account, the average number of sides and neighbors of the edge fragments was 4.1 and 5.8, respectively. This reveals that the edge fragments also presented a hierarchical structure with four sides and six neighbors (Ref 9). The above-mentioned two aspects, i.e., the differences in both the preferential cracking orientation and the domain size between center fragments and edge fragments, are defined as the edge effect on intrasplat cracking for the case of polycrystalline splats.

Crack Patterns of Polycrystalline LZ and TiO₂ Splats

When the edge effect in polycrystalline YSZ splats was investigated, a question arose as to whether this edge effect was due to polycrystallinity. To identify the contributing factor of polycrystallinity, two random splat-substrate combinations, i.e., TiO₂-Si and LZ-Al₂O₃ were investigated. Both surface morphologies are shown in Fig. 3. As compared to the polycrystalline YSZ splats, a lesser edge effect developed. Indeed, the cracks for the edge fragments showed preferential orientation, i.e., either perpendicular or parallel to the local edge. However, the edge fragments were somewhat smaller than the center fragments for LZ splats on the single-crystal Al₂O₃ substrate, which is different from the TiO₂ splats on the single-crystal Si substrate and the YSZ splats on the YSZ substrate. Appreciably, larger patterns always appear where the wider cracks exist.

Edge Effect of Crack Patterns for Single-Crystal Splats

As comparisons with polycrystalline splats, crack morphologies of corresponding single-crystal splats were researched. As expected, the results also revealed clear edge effects at the periphery.

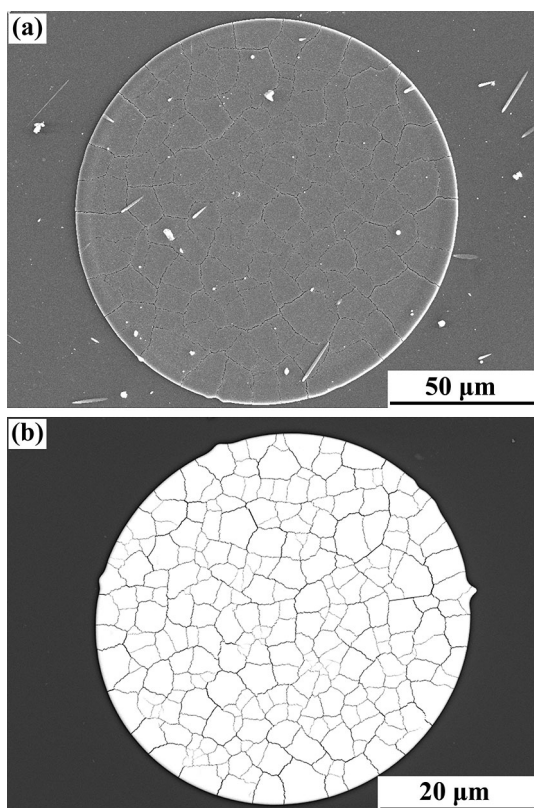


Fig. 3 Surface morphologies of TiO₂ splats on (a) single-crystal Si substrate and (b) LZ splats on single-crystal Al₂O₃ substrate

Crack Patterns of Single-Crystal TiO₂ Splats

To eliminate the influence of polycrystallinity, single-crystal splats of the three materials used in this study were prepared by deliberately selecting the substrate material. Thus, TiO₂ splats were deposited on a single-crystal TiO₂ substrate. Electron back-scatter diffraction (EBSD) orientation maps (Fig. 4c) revealed that epitaxial growth with $\langle 001 \rangle$ orientation readily occurred. Similar to the polycrystalline TiO₂ splats shown in Fig. 3(a), the crack patterns of the single-crystal TiO₂ splats shown in Fig. 4 also presented obvious preferential orientation, i.e., centripetal cracking roughly perpendicular to local edge. Because of the anisotropic characteristic of single crystals, cracking tends to occur along specific orientations (Ref 9). As a result, the intrasplat cracks tended to be perpendicular to each other in the splats. It was also found that almost all of the vertical cracks in the single-crystal splats approached the substrate edge (oriented by $\langle 100 \rangle$ direction) at a 45° angle, which revealed $\langle 110 \rangle$ orientation for vertical cracks. Because of the rough surface morphology, a fair number of narrow vertical cracks (covered by the ridges) are not visible. In addition, the patterns at the periphery were larger than those in the center, which is clearly shown in Fig. 4(a). Meanwhile, substrate delamination at the edges is clearly observed in Fig. 4(b). These results revealed an obvious edge effect in single-crystal TiO₂ splat.

Crack Patterns of Single-Crystal YSZ Splats

Single-crystal YSZ splats were also prepared on a single-crystal YSZ substrate, and the results are shown in Fig. 5. Epitaxial growth along $\langle 001 \rangle$ orientation and vertical cracks along $\langle 110 \rangle$ orientation were clearly found. This is consistent with the close-packed direction of face-centered cubic (FCC) YSZ crystals because of the anisotropic characteristic of single crystals. Similar to single-crystal TiO₂ splat, the single-crystal YSZ splats also presented preferential orientation, i.e., centripetal cracking roughly perpendicular to the local edge. As compared to the polycrystalline splats, the single-crystal YSZ splats shown in Fig. 5 show an exceptionally distinct surface morphology. The splat delamination cracks preferred to initiate from the periphery and then propagate throughout the whole single-crystal splat, forming elongated strips, as shown in Fig. 5(a). Consequently, the strips had a width of approximately 10 μm but a length of 40–80 μm. Moreover, a fair number of splats detached at the periphery without perpendicular cracks, as shown in Fig. 5(b). In addition, spalling of splats coated with a thin substrate lamella was also widely found, as shown in Fig. 5(c). Therefore, the edge effect of the preferential cracking orientation of single-crystal YSZ splats was evidently similar to that of

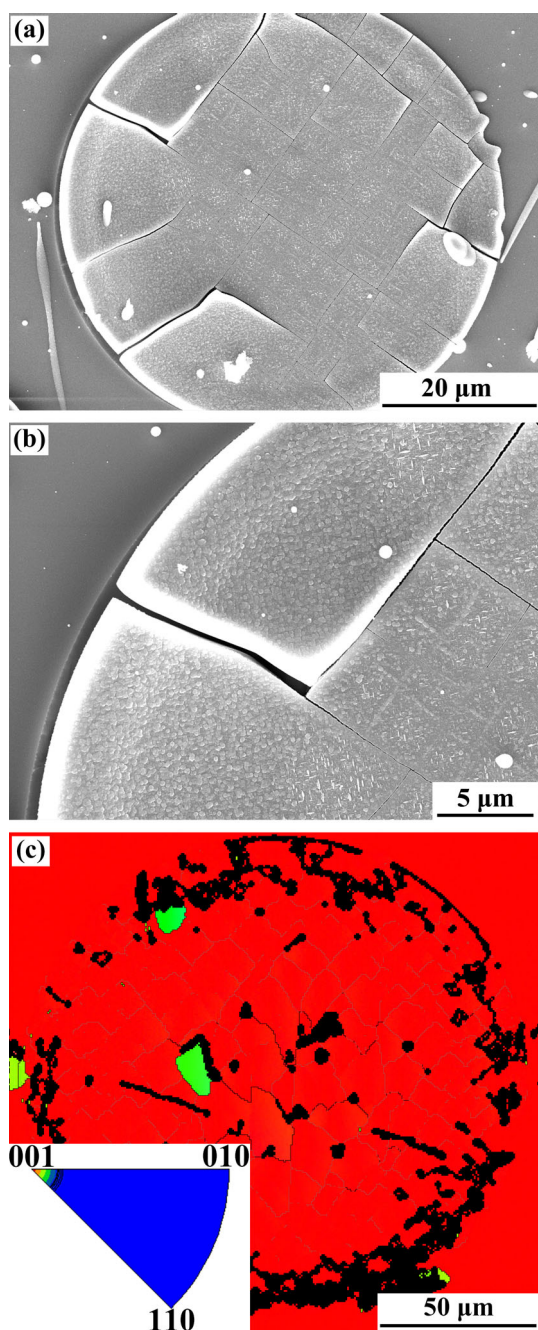


Fig. 4 Surface morphologies of TiO_2 single-crystal splats on TiO_2 single-crystal substrate. (a) The pattern size at the periphery was much larger than that at the center. (b) An apparent substrate delamination occurred at the splat edge. (c) Orientation maps by EBSD revealed epitaxial growth

polycrystalline splats, whereas the edge effect on fragment size could not be further evaluated for the single-crystal YSZ splats because there were so few fragments. However, all of these features might be deteriorated by the anisotropy of single-crystal material. Therefore, it was occasionally found that several small patterns appeared at the periphery.

Crack Pattern of Single-Crystal LZ Splats

Single-crystal LZ splats were also obtained on a single-crystal YSZ substrate, and the results are shown in Fig. 6. Similar to the case of YSZ single crystals, epitaxial growth with $\langle 001 \rangle$ orientation and vertical cracks with $\langle 110 \rangle$ orientation were widely found. As expected, most cracks on the periphery propagated along the radial direction, as shown in Fig. 6(a). As a result, peculiar elongated strips formed with length on order of $30 \mu\text{m}$. Benefiting from a shielding plate over the substrate and high scan speed of spray gun (1200 mm/s), almost no splashing and overlapping in splats occurred. Also, the splat/substrate interface was easily distinguished by energy detecting spectra (EDS; the results are shown in Fig. 11 in “Appendix”) because of the element differences between the splat (LZ) and substrate (YSZ). Substrate delamination on the periphery is clearly shown in Fig. 6(b). Moreover, it was found that most of the patterns on the periphery were delaminated from the splat/substrate interface, as shown in Fig. 6(a) and (b). When comparing the fragment size on the periphery with that in the center region, the edge effect on fragment size should be clearly identified for LZ single-crystal splats.

In short, both the polycrystalline splats and single-crystal splats present evidently edge effect, i.e., preferential cracking orientation and the domain size difference between center fragments and edge fragments. In addition, it is also clearly observed delamination at/beneath the splat/substrate interface in periphery region for single-crystal splats.

Edge Effect Based on Mechanical Analysis

The experimental results clearly demonstrated that both polycrystalline splats and single-crystal splats showed obvious edge effects. Because free edges significantly contribute to stress redistribution and thus change the mechanical behavior of edges, mechanical analysis is quite necessary to identify the influence of the edge effect. The edge effect was investigated in terms of the stress characteristics on the substrate, the whole splat, and splat segments using mechanical analysis.

Free-Edge Effect on Substrate Stress

First, mechanical analysis of the free-edge effect on substrate stress was carried out. Stresses are always concomitant with a multilayer structure, because of either intrinsic built-in stresses in films or coatings (according to the processes by which the films or coatings are formed, herein referred to as “splats”) or because of thermal expansion mismatch between the splat and the substrate.

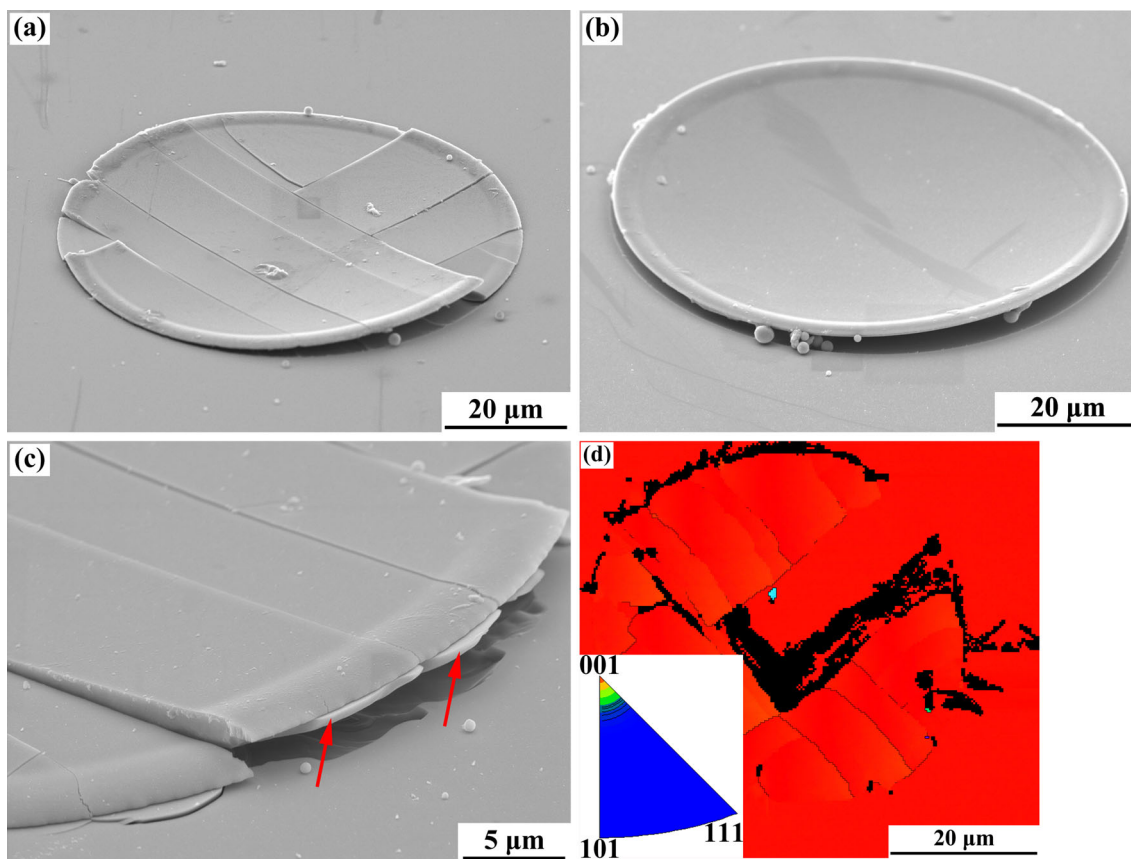


Fig. 5 Surface morphologies of YSZ splats on single-crystal YSZ substrate showing (a) the strip-like fragments, (b) a whole splat delaminated from the splat edges without perpendicular cracks, and

(c) thin substrate lamellae removed concomitantly with delaminated patterns, as marked by the red arrows. (d) Orientation maps by EBSD revealing epitaxial growth

Such stresses are generally quite small in the substrate by virtue of its much larger thickness than the thicknesses of the overlays on a macroscale (Saint-Venant’s principle). In the neighborhood of discontinuities of the splats, however, very large localized stresses can occur in the substrate due to the asymmetrical deformation of the substrate resulting from the film “edge forces.”

On the basis of a concentrated force model, a simple analytical solution to the stress distribution in the substrate can be obtained, such that the tensile stress and shear stress components in the x direction in the substrate, as shown in Fig. 7(a), σ_x^s and τ_{xy}^s , are given by (Ref 10-15),

$$\sigma_x^s(x, y) = \frac{-2F_x}{\pi} \left\{ \frac{(x+l)^3}{[(x+l)^2+y^2]^2} - \frac{(x-l)^3}{[(x-l)^2+y^2]^2} \right\}$$

$$\tau_{xy}^s(x, y) = -\frac{2F_x}{\pi} \frac{x^2y}{(x^2+y^2)^2} \tag{Eq 1}$$

where F_x is the concentrated line force tangential to the boundary of a half-space. The stress σ_x^s at the interface is thus reduced to

$$\sigma_x^s(x, 0) = \frac{-2F_x}{\pi l} \left(\frac{1}{x/l+1} - \frac{1}{x/l-1} \right) \tag{Eq 2}$$

Normalizing the substrate stress gives

$$N = \sigma_x^s(x, 0)/(-2F_x/\pi l)$$

$$N' = \text{sign}(N) \cdot \log_{10}|N| \tag{Eq 3}$$

where the sign function reads $\text{sign}(N) = \begin{cases} 1, & N > 0 \\ -1, & N < 0 \end{cases}$.

The results are plotted in Fig. 7(b). It was clearly found that the stress distribution in the substrate was divided into two regions: One referred to as “inner region” (the domain under the film) and the other referred to as “outer region” (the domain outside the film edge). The sign of the substrate stress in the inner region (compressive stress) is opposite to that of F_x because it is employed to balance the film deformation. Inversely, the stress of the substrate in outer region is due to asymmetrical deformation. In brief, the stress distribution in the substrate is extremely inhomogeneous, and there is an evident singularity for the substrate stress on the splat edge.

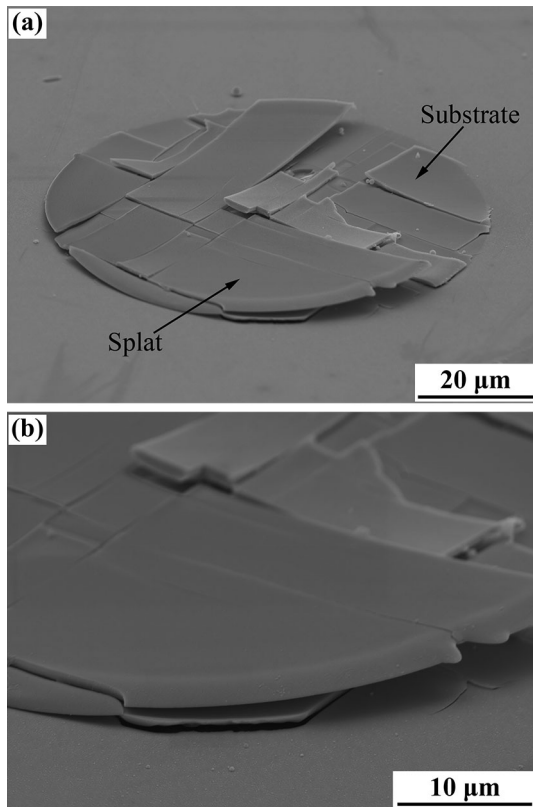


Fig. 6 Surface morphologies of LZ splats on single-crystal YSZ substrate at (a) low magnification and (b) high magnification. Interfacial delamination in conjunction with substrate spallation is clearly observed in (a) and (b)

Free-Edge Effect on the Whole-Splat Stress

Generally, an individual disk-shaped splat is divided into small segments by intrasplat cracks. However, before intrasplat cracking occurs, the initial disk-shaped splat serves as the whole splat. To reveal the edge effect on a whole splat, the concept of whole-splat stress is developed in this section. It has been reported that the origin and nature of stress in a film (herein referred to as a “splat”) and a substrate can be considered equivalent when the stresses and strains are calculated (Ref 15, 16). The stresses in thermally sprayed ceramic coatings originate from splat cooling shrinkage strain, which are thus equivalent to stresses due to thermal expansion mismatch with zero thermal expansion of the substrate. The simple beam theory in the mechanics of materials can be used to solve thermal mismatch problems under steady-state condition. The strain and stress in a splat can be expressed by (the details are shown in “Appendix”)

$$\epsilon_f^t = -\frac{6E_f h_f}{E_s h_s^2} \Delta\alpha\Delta T \cdot \left(y + \frac{h_s}{2}\right) \tag{Eq 4}$$

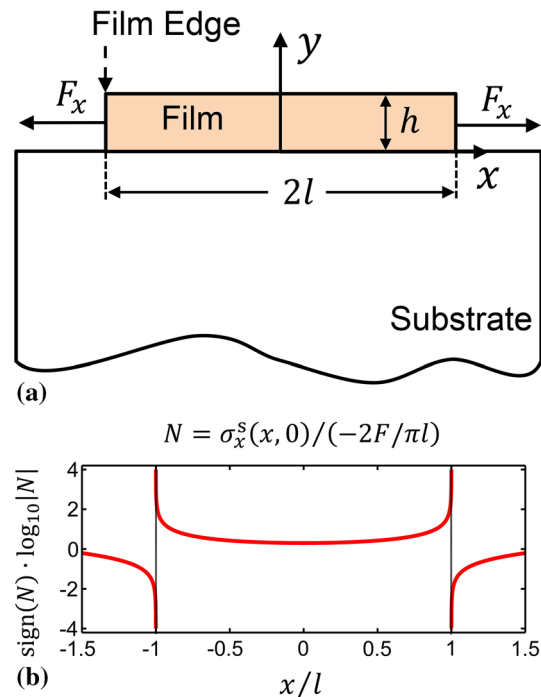


Fig. 7 Substrate stress distribution and the film/substrate architecture. (a) Diagram of free splat edges located in the interior substrate. (b) Distribution of normalized substrate stress $[\sigma_x^s(x, 0)/(-2F/\pi l)]$ related to the normalized position (x/l)

$$\sigma_f^t = E_f \left[-\frac{6E_f h_f}{E_s h_s^2} \Delta\alpha\Delta T \cdot \left(y + \frac{h_s}{2}\right) - \alpha_f \Delta T \right]. \tag{Eq 5}$$

where E_f and E_s is Young’s modulus of the splat and substrate, respectively. Moreover, h_f and h_s are the thickness of the splat and substrate, respectively. The value y and $\Delta\alpha$ denote the height to the splat/substrate interface and the equivalent thermal expansion mismatch between the splat and substrate, respectively. Because the thickness ratio of the splat to substrate is nearly equal to zero, Eq 5 can be further reduced to $\sigma_f^t = -E_f \alpha_f \Delta T$, which reveals that the residual stress in a splat is nearly independent of splat thickness and that the bending can be neglected in the case of infinite substrate thickness.

It is important to note that these effects refer to stresses far away from the edges of a multilayer system. However, at the edges of the system, satisfaction of the free surface condition is also required. This can be achieved via a superposition procedure. First, the remote stresses, σ_f^t and σ_s^t , are assumed to be distributed throughout the length of the system. Then, stresses of the same value but opposite sign, i.e., $-\sigma_f^t$ and $-\sigma_s^t$, are applied at the corresponding positions along the edges. It is important to realize that the net resultant force from the imaginary applied stresses is zero because the assumed stresses satisfy the force equilibrium condition. The stress field in the edge region is thus the superposition of the assumed stress fields and those due

to the imaginary applied stresses. Because of the complexity of the problem, exact closed-form solutions to stress fields in the edge region are difficult to obtain. However, the moment and shearing force at the free edge due to the applied stresses can be readily derived for an interface as follows

$$M = \int_0^{h_f} \sigma_f^t y dy \approx -E_f \alpha_f \Delta T \cdot h_f^2 / 2 \tag{Eq 6}$$

$$V = \int_0^{h_f} \sigma_f^t dy \approx -E_f \alpha_f \Delta T h_f \tag{Eq 7}$$

In the edge region, the additional peeling stresses and shear stresses at the interface are thus induced by the moment and force given by Eq 6 and 7, respectively. Because of the complexity of the problem, exact closed-form solutions to peeling stress and shear stress distribution are exceedingly difficult to obtain. For simplicity, the apparent average value of the interfacial peeling stress and shear stress is evenly imposed at a finite zone near the edge with an order of λh_f . They thus follow

$$\begin{aligned} \tau(x) &= -E_f \alpha_f \Delta T / \lambda \\ p(x) &= -2(E_f \alpha_f \Delta T) / \lambda^2 \end{aligned} \tag{Eq 8}$$

If taking typical conditions of $\lambda \approx 4$, $E_f \approx 200$ GPa and $\alpha_f \Delta T \approx 2\%$ into account, the average shear stress and peeling stress at the interface are further reduced to

$$\begin{aligned} \tau(x) &\approx -E_f \alpha_f \Delta T / 4 \approx 1 \text{ GPa} \\ p(x) &= -(E_f \alpha_f \Delta T) / 8 \approx 500 \text{ MPa} \end{aligned} \tag{Eq 9}$$

It is obvious that very large average values for the shear stress and peeling stress are produced because of free edges. Furthermore, the inhomogeneous distribution of the shear stress and peeling stress should also be discussed. To show the change in the stress along the radius, the stress fields in an elongated bimaterial beam by Suhir (Ref 17-19) under the assumption that longitudinal displacements at the interface dictate the function forms are employed as follows,

$$\begin{aligned} u_1(x) &= \alpha_1 \Delta T x - \frac{1 - \nu_1^2}{E_1 h_1 b} \int_0^x Q(\xi) d\xi + \kappa_1 q(x) + \frac{h_1}{2} \int_0^x \frac{d\xi}{\rho(\xi)} \\ u_2(x) &= \alpha_2 \Delta T x + \frac{1 - \nu_2^2}{E_2 h_2 b} \int_0^x Q(\xi) d\xi - \kappa_1 q(x) - \frac{h_2}{2} \int_0^x \frac{d\xi}{\rho(\xi)} \end{aligned} \tag{Eq 10}$$

where $u_1(x)$ and $u_2(x)$ denote the displacements of the lower surface of material 1 (herein referred to as “film”) and upper surface of material 2 (herein referred to as “substrate”), respectively. Moreover, b is the strip width, $Q(\xi)$ is the normal stress at a neutral axis, and $\rho(x)$ is the

radius of curvature. Additionally, $q(x)$ is the shearing force per unit plate length, and

$$\kappa_1 = \frac{2(1 + \nu_1) h_1}{3E_1 b}, \quad \kappa_2 = \frac{2(1 + \nu_2) h_2}{3E_2 b} \tag{Eq 11}$$

are the coefficients of interfacial compliance, which are widely used to approximate the mathematical relationship between the shear stress and displacement at an interface. The main contribution of Suhir’s work is additional consideration of the influence of the actual nonuniform distribution of forces $Q(x)$ and assuming that the corresponding corrections are directly proportional to the shearing force at the interface (the third term in Eq 10).

Using the condition $u_1(x) = u_2(x)$ of the displacement compatibility and elongated beam bending theory, the interfacial peeling stress $p(x)$ and shear stress $\tau(x)$ consequently dictate the function form as

$$\tau(x) = \frac{\Delta \alpha \Delta T}{K \kappa \cosh(Kl)} \sinh(Kx) \tag{Eq 12}$$

$$p(x) = \frac{\mu \Delta \alpha \Delta T}{\kappa \cosh(Kl)} \cosh(Kx) \tag{Eq 13}$$

where the quantities κ , K , and μ are geometric factors related to E , ν , and h . In the case of an elongated bimaterial beam when the Kl value is great, these stresses can be further expressed as

$$\tau(x) = \tau_{\max} e^{-K(l-x)} \tag{Eq 14}$$

$$p(x) = p_{\max} e^{-K(l-x)} \tag{Eq 15}$$

Equation 14 and 15 demonstrate that both the shear stress and peeling stress at the interface present quick exponential decay to the center. If taking the huge average values for the shear stress and peeling stress (Eq 9) into account, it can be concluded that singular shear stress and peeling stress exist in the splat edge region because of the edge effect.

Edge Effect on Splat Segment Stress

When the whole disk-shaped splat is divided into small segments by intrasplat cracks, each segment will also present an edge effect because of the new edges produced by the intrasplat cracks. This is similar to film domains divided by channeling cracks. These channeling cracks consequently create more “free edges,” giving rise to stress redistribution in the film, as shown in Fig. 8(a). In addition, curling of the pattern edges in the center region is also clearly observed, as shown in Fig. 6(a). Therefore, it is necessary to identify the edge effect on pattern cracking in the film.

In this section, the ideal model shown in Fig. 8 is addressed. Because the thickness of the splat is much

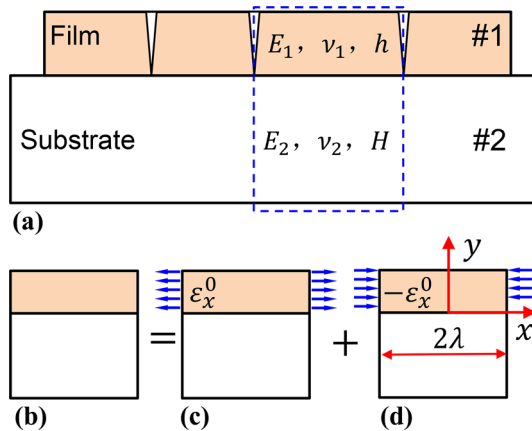


Fig. 8 Solution to segment stress after pattern cracking via superposition principle. (a) A brittle film on a thick substrate with arrays of perpendicular cracks. (b) The marked section between two cracks. (c) The strain is assumed to be uniformly distributed in the film before cracking. (d) An applied stress of opposite sign is imposed on the free edge to relax the edge stress. The stress distribution in (b) is equivalent to the superposition of stress distribution in (c) and (d)

smaller than its length and the top surface is free, generally the top surface of the splat remains approximately flat in the case of no delamination. This is in reasonable accordance with the preceding results, in which the influence of bending on stress distribution was neglected.

The plane strain problem is thus adopted. Herein only the stress in x direction is considered because of the total equivalence symmetry in the x and z directions.

The equilibrium equation (Navier equations in elasticity) in the absence of a body force in the x direction can be written as

$$\frac{\partial \sigma_x}{\partial x} + \frac{\partial \tau_{xy}}{\partial y} = 0 \tag{Eq 16}$$

In conjunction with constitutive law in elasticity and the method of separation of variables, the displacement in splat dictates the function form (Ref 20, 21)

$$u_x(x,y) = \left(A_1 e^{cx/h} + A_2 e^{-cx/h} \right) \left[B_1 \sin(dy/h) + B_2 \cos(dy/h) \right] \tag{Eq 17}$$

where $A_1, A_2, B_1,$ and B_2 are coefficients to be determined by the boundary conditions. The existence of h is because of dimensional consideration. Moreover, the correlative dimensionless coefficients, c and $d,$ satisfy the equation $d = c \cdot \sqrt{E_1/\mu_1}.$

Considering the boundary conditions, i.e., the geometric symmetry in $x = 0$ direction and the stress free in $y = h$ and $x = \pm\lambda$ direction, Eq 17 can be reduced to

$$u_x(x,y) = A \sinh(cx/h) \cos[d(1 - y/h)] \tag{Eq 18}$$

where the dimensionless coefficient A satisfies the equation

$$A = -\sqrt{\frac{E_1}{\mu_1}} \frac{h \varepsilon_x^0}{\cosh(c\lambda/h) \sin d}.$$

It is reported that the comparison of the energy release rate with the exact solution provides (Ref 20, 22)

$$c = \frac{2}{\pi g(\alpha, \beta)}; \quad d = \sqrt{\frac{E_1}{\mu_1}} c \tag{Eq 19}$$

where the quantity $g(\alpha, \beta)$ dictates the function form (Ref 20)

$$g(\alpha, \beta) \approx \frac{1.258 - 0.40\alpha - 0.26\alpha^3 - 0.30\alpha^4}{1 - \alpha} \tag{Eq 20}$$

The nondimensional quantity α can be expressed by (Ref 23-26) $\alpha = \frac{\bar{E}_1 - \bar{E}_2}{\bar{E}_1 + \bar{E}_2}.$

Consequently, the total displacement and stress shown in Fig. 8(b) are equivalent to the superposition of displacement and stress shown in Fig. 8(c) and (d), which dictate the function forms

$$u_x(x,y) = \varepsilon_x^0 x + A \sinh(cx/h) \cos[d(1 - y/h)] \tag{Eq 21}$$

$$\sigma_x = \bar{E}_1 (\varepsilon_x^0 + A c / h \cosh(cx/h) \cos[d(1 - y/h)]) \tag{Eq 22}$$

$$\tau_{xy} = \mu_1 A d / h \sinh(cx/h) \sin[d(1 - y/h)] \tag{Eq 23}$$

The shear stress at the interface and the average tensile stress in the film are thus

$$\tau_{xy}(x,0) = -\bar{E}_1 \varepsilon_x^0 \cdot c \cdot \frac{\sinh(cx/h)}{\cosh(c\lambda/h)} \tag{Eq 24}$$

$$\bar{\sigma}_x = \bar{E}_1 \varepsilon_x^0 \left(1 - \frac{\cosh(cx/h)}{\cosh(c\lambda/h)} \right) \tag{Eq 25}$$

In the case of a film having identical properties with the substrate, namely $\alpha = 0$ and $c = 0.5,$ the normalized shear stress at the interface and the tensile stress in the film, i.e., $\tau_{xy}(x,0)/(-\bar{E}_1 \varepsilon_x^0 \cdot c)$ and $\bar{\sigma}_x/(\bar{E}_1 \varepsilon_x^0)$ related to the normalized position, $x/h,$ is plotted as shown in Fig. 9(a) and (b), respectively. It is obvious that the shear stress presents exponential decay from the fragment edge to the center, and the maximum value is obtained in the position of $x = \lambda$ and $y = 0,$ which provides

$$\tau_{\max} = -\bar{E}_1 \varepsilon_x^0 \cdot c \cdot \tanh(c\lambda/h) \tag{Eq 26}$$

In this case, the maximum shear stress is comparable to the tensile stress. In addition, there also exists a moment as a result of the imaginary stress, shown in Fig. 8(d), which gives rise to a self-equilibrium peeling stress distributed along the interface in the edge region. Both peeling stress and shear stress reached maximum values at the edge and contributed to interface cracking.

As compared to shear stress at the interface, the tensile stress in the fragments presented exponential decay from

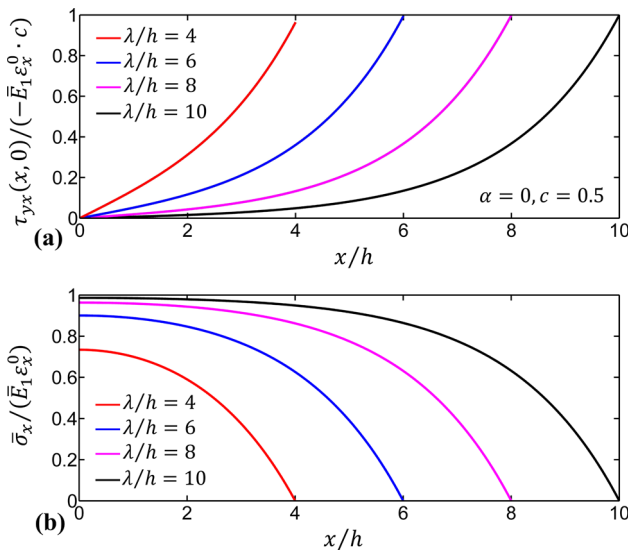


Fig. 9 (a) Normalized shear stress and (b) normal stress of segment at interface related to normalized position (x/h)

the center to the periphery, as shown in Fig. 9(b), which means effective relief occurs because of the edge effect. Further intrasplat cracking probably develops in the center region in the case of large-enough patterns (namely a large-enough λ value). Inversely, shear stress always reaches a peak at the edge, no matter how large the patterns are.

In brief, there is an edge effect in mechanics where the film rests on the inner region of the substrate. Concretely, the edge effect dictates that singular tensile stresses develop at the film edge in the substrate because of geometrical asymmetry, and tremendous interfacial peeling stress and shear stresses are induced in the film. Additionally, considerable interfacial peeling stress and shear stresses are induced in crack patterns because of the edge effect. All these singular stresses magnify the possibility and tendency of film cracking.

Discussion

The edge effect was detected through both experimental observation and mechanical analysis. Naturally, a correlation between experimental observation and mechanical analysis was expected. Among the detailed aspects of the edge effect, the most important and common aspect was that all edge intrasplat cracks tended to be locally perpendicular to the splat edge. This can be understood as follows. Based on the previous mechanical analysis, the singular peeling stress and shear stress due to the edge effect were elaborated. However, it should be noted that the tensile stress in the crack patterns decreased concomitantly via relief of the free edges when tremendous

shear stress and peeling stress were produced. Additionally, the film in this study was actually a disk-shaped splat, where the tensile stress was along the axial and circumferential direction in a polar coordinate system. Because of the zero stress state at the boundary and stress continuity in the splat, the tensile stress along the radial direction was effectively released in the finite zone (as shown in Eq 25 and Fig. 9b). However, the tensile stress along the circumferential direction was preserved because of the lack of a free edge. Consequently, the intrasplat cracking tended to occur along the radial direction, as widely shown in Fig. 2-6, for both polycrystalline splats and single-crystal splats.

In all single-crystal splats, transverse delamination at or below the splat/substrate interface was clearly observed (Fig. 4-6), which was well consistent with singular peeling stress and shear stress at the edge in the mechanical analysis (Eq 8, 24 and Fig. 9a). As a result, the domain sizes of the edge fragments were larger than those in the center region (Fig. 4-6). However, the difference was not quite distinct, which seems to go counter to the mechanical analysis. Based on previous mechanical analysis, the singular peeling stress and shear stress due to the edge effect were elaborated. From the perspective of strength theory, cracking would be more likely to occur if the shear stress and peeling stress exceeded the fracture strength. However, fracture is related not only to stress but also to energy differences (Ref 9, 27, 28). On a more microscopic scale, fracture is significantly influenced by the statistical distribution of microdefects (crack sources). In short, the two most essential factors influencing cracking behavior are cracking motivation (stress condition) and cracking resistance such as the elastic anisotropy in the single-crystal material and defect quantities in polycrystalline material. Where cracking initiates and propagates generally depends on the maximum ratio between cracking motivation and resistance, i.e., either on greatest motivation or the least resistance (Ref 9, 28). As expected, we found a clear edge effect in single-crystal TiO_2 splats, while some deviations were found in single-crystal YSZ and LZ splats. Consequently, the competition between the edge effect and cracking resistance needs to be further addressed.

For polycrystalline splats, the number of defects in plane (such as weak grain boundaries; it is reported that the different types of splats mentioned previously are preferential to intergranular cracking) was significant, which is in accordance with the phenomenon that the patterns with larger sizes in weak hierarchical polycrystalline LZ splats were concomitant with wider cracks, which are the positions with foremost cracking (Ref 9). Consequently, it is reasonable that the strain energy would be released via perpendicular cracking rather than via transverse delamination. Without these deteriorations, both single-crystal

and polycrystalline splats present preferential intrasplat cracking orientation and different fragment sizes between edge and center region resulting from edge effect. Conceptually, utilizing edge effect to tailor the crack topology (as shown in Fig. 5b) and even the coating structure could be a potential future work.

Conclusions

To explore the edge effect on intrasplat cracking of thermally sprayed ceramic splats, the crack morphologies of splats were experimentally observed and investigated using mechanical analysis. Both the polycrystalline splats and single-crystal splats presented evident edge effects, i.e., preferential cracking orientation and domain size differences between the center fragments and the edge fragments. In addition, delamination at/beneath the splat/substrate interface at the periphery was often observed for single-crystal splats. The mechanical analysis showed that both singular normal stress in the substrate and huge peeling stress and shear stresses at the interface were induced. These huge stresses significantly contributed to the delamination at/beneath the splat/substrate interface at the edge region. Moreover, effective relief of the tensile stress in a splat was discussed, which was obviously related to the preferential cracking orientation. The good correspondence of the edge effect between experimental observation and mechanical analysis was elaborated.

Acknowledgments The present project is supported by National Basic Research Program (No. 2013CB035701), the Fundamental Research Funds for the Central Universities, and the National Program for Support of Top-notch Young Professionals.

Appendix

The constitutive law in regard to thermal strain without consideration of bending problem reads

$$\begin{aligned} \epsilon_f^0 &= \frac{\sigma_f^i}{E_f} + \alpha_f \Delta T = \epsilon_f^i + \alpha_f \Delta T \\ \epsilon_s^0 &= \frac{\sigma_s^i}{E_s} + \alpha_s \Delta T = \epsilon_s^i + \alpha_s \Delta T \end{aligned} \tag{Eq 27}$$

where ϵ_f^0 and ϵ_s^0 are the uniform strain of the splat and substrate without consideration of bending, respectively. Moreover, σ_f^i and σ_s^i are the uniform stress of the splat and substrate, respectively. Using the condition of the strain compatibility at the film/substrate interface gives

$$\epsilon_f^i - \epsilon_s^i = (\alpha_s - \alpha_f) \Delta T = \Delta \alpha \Delta T \tag{Eq 28}$$

The force balance of the whole bimaterial beams dictates

$$E_f \epsilon_f^i h_f + E_s \epsilon_s^i h_s = 0 \tag{Eq 29}$$

Combination of Eq 28 and 29 gives

$$\begin{aligned} \epsilon_f^i &= \frac{E_s h_s \Delta \alpha \Delta T}{E_f h_f + E_s h_s} \\ \epsilon_s^i &= \frac{-E_f h_f \Delta \alpha \Delta T}{E_f h_f + E_s h_s} \end{aligned} \tag{Eq 30}$$

The moments due to uniform strain component, M^i , can thus be expressed as

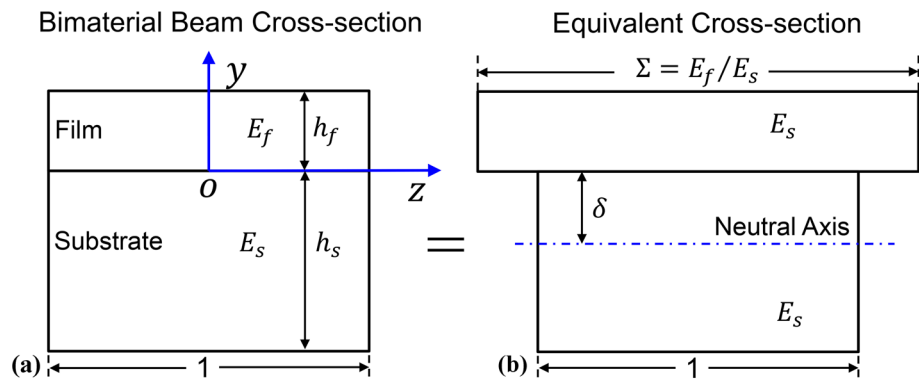
$$M^i = \int_0^{h_f} E_f \epsilon_f^i (y - \delta) dy + \int_{-h_s}^0 E_s \epsilon_s^i (y - \delta) dy \tag{Eq 31}$$

where δ is the location of the neutral axis composite beam. The quantity δ was calculated on the assumption of equivalent cross section (Ref 25) as shown in Fig. 10, which was defined as

$$\delta = \frac{y_f A_f + y_s A_s}{A_f + A_s} \tag{Eq 32}$$

where y_f and y_s are the location of the neutral axis of film and substrate, respectively. The quantities A_f and A_s are the equivalent cross-sectional area of film and substrate, as shown in Fig. 10(b), respectively. Therefore, δ can further be reduced to

Fig. 10 Procedure for finding the location of the neutral axis of a composite beam. (a) Actual cross section of bimaterial beam and (b) equivalent cross section of bimaterial beam on the assumption of equal bending stiffness



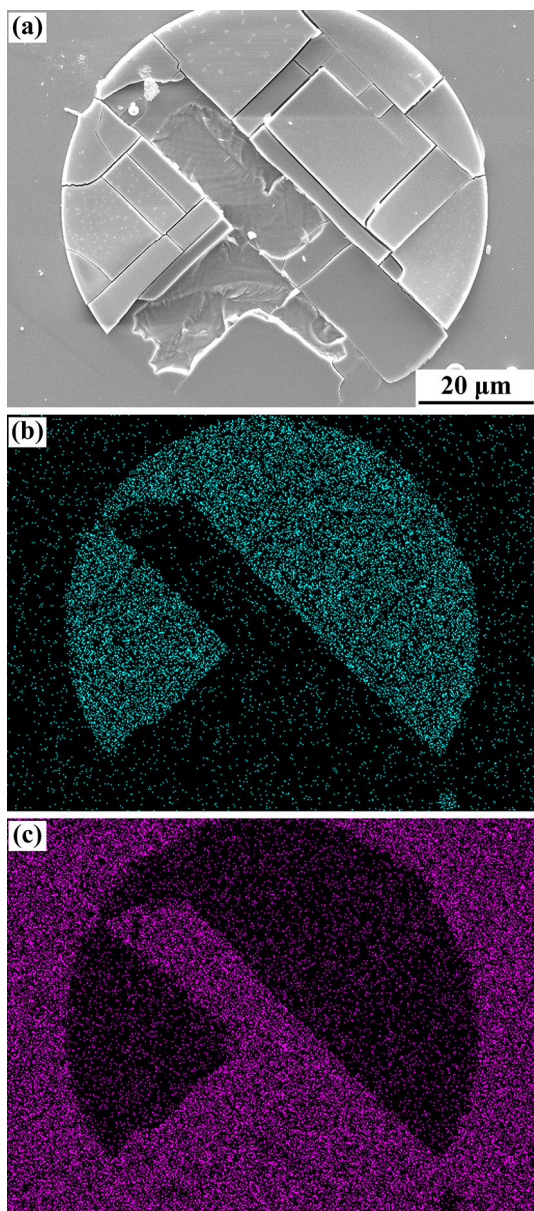


Fig. 11 The SEM (a) and EDS (b, c) morphology of single-crystal LZ splats deposited on single-crystal YSZ substrate. The element shown in (b) and (c) was lanthanum (La) and yttrium (Y) corresponding to LZ splats and YSZ substrate, respectively

$$\delta = \frac{E_f h_f^2 - E_s h_s^2}{2(E_f h_f + E_s h_s)} \tag{Eq 33}$$

To balance the moment M^i , an extra moment M^b is required, which in return gives rise to stress redistribution in bimaterial beam.

The pure bending strain due to M^b dictates the function form

$$\varepsilon^b = \frac{y - \delta}{r} \tag{Eq 34}$$

where r is the radius of curvature for neutral axis of composite beam.

The bending moment, M^b , related to the pure bending strains ε^b , can be expressed as

$$M^b = \int_{-h_s}^0 E_s \frac{(y - \delta)^2}{r} dy + \int_0^{h_f} E_f \frac{(y - \delta)^2}{r} dy \tag{Eq 35}$$

The moment balance of the whole bimaterial beam follows $M^i + M^b = 0$, which in conjunction with Eq 31, 34, and 35 dictates

$$\frac{1}{r} = \frac{3}{2} \cdot \frac{E_s \varepsilon_s^i h_s (h_s + 2\delta) - E_f \varepsilon_f^i h_f (h_f - 2\delta)}{E_s h_s (h_s^2 + 3h_s \delta + 3\delta^2) + E_f h_f (h_f^2 - 3h_f \delta + 3\delta^2)} \tag{Eq 36}$$

The total strain in the film (the upper beam) can thus be expressed as

$$\varepsilon_f^t = \alpha_f \Delta T + \varepsilon_f^i + \varepsilon_f^b = \alpha_f \Delta T + \frac{E_s h_s \Delta \alpha \Delta T}{E_f h_f + E_s h_s} + \frac{y - \delta}{r} \tag{Eq 37}$$

In the present study,

$$\eta = h_f / h_s = 1/500 \rightarrow 0$$

$$\lim_{\eta \rightarrow 0} \varepsilon_f^i = (\alpha_s - \alpha_f) \Delta T$$

$$\lim_{\eta \rightarrow 0} \delta = -\frac{h_s}{2}$$

$$\lim_{\eta \rightarrow 0} \frac{1}{r} = \frac{-6E_f h_f}{E_s h_s^2} \Delta \alpha \Delta T = 0 \tag{Eq 38}$$

Therefore, the strain and stress in the film can be reduced to

$$\varepsilon_f^t = -\frac{6E_f h_f}{E_s h_s^2} \Delta \alpha \Delta T \cdot \left(y + \frac{h_s}{2} \right)$$

$$\sigma_f^t = E_f \left[-\frac{6E_f h_f}{E_s h_s^2} \Delta \alpha \Delta T \cdot \left(y + \frac{h_s}{2} \right) - \alpha_f \Delta T \right] \tag{Eq 39}$$

References

1. A. Ohmori and C.J. Li, Quantitative Characterization of the Structure of Plasma-Sprayed Al_2O_3 Coating by Using Copper Electroplating, *Thin Solid Films*, 1991, **201**(2), p 241-252
2. R. Mcpherson, A Model for the Thermal-Conductivity of Plasma-Sprayed Ceramic Coatings, *Thin Solid Films*, 1984, **112**(1), p 89-95
3. S. Kuroda, T. Dendo, and S. Kitahara, Quenching Stress in Plasma-Sprayed Coatings and Its Correlation with the Deposit Microstructure, *J Therm Spray Techn*, 1995, **4**(1), p 75-84
4. S. Kuroda and T.W. Clyne, The Quenching Stress in Thermally Sprayed Coatings, *Thin Solid Films*, 1991, **200**(1), p 49-66
5. S. Kuroda, T. Fukushima, and S. Kitahara, Significance of Quenching Stress in the Cohesion and Adhesion of Thermally Sprayed Coatings, *J Therm Spray Techn*, 1992, **1**(4), p 325-332

6. C.J. Li and A. Ohmori, Relationships Between the Microstructure and Properties of Thermally Sprayed Deposits, *J Therm Spray Techn*, 2002, **11**(3), p 365-374
7. S. Rangarajan and A.H. King, Non-destructive Evaluation of Delamination in Ceramic Thin Films on Metal Substrates by Scanning Electron Microscopy, *Thin Solid Films*, 2001, **385**(1-2), p 22-28
8. T. Chraska and A.H. King, Effect of Different Substrate Conditions upon Interface with Plasma Sprayed Zirconia-A TEM Study, *Surf Coat Tech*, 2002, **157**(2-3), p 238-246
9. L. Chen, G.-J. Yang, C.-X. Li, and C.-J. Li, Hierarchical Formation of Intrasplat Cracks in Thermal Spray Ceramic Coatings, *J Therm Spray Techn*, 2016, **25**(5), p 959-970
10. I. Dewolf, J. Vanhellefont, A. Romanorodriguez, H. Norstrom, and H.E. Maes, Micro-Raman Study of Stress-Distribution in Local Isolation Structures and Correlation with Transmission Electron-Microscopy, *J. Appl. Phys.*, 1992, **71**(2), p 898-906
11. A. Atkinson, T. Johnson, A. Harker, and S. Jain, Film Edge-induced Stress in Substrates and Finite Films, *Thin Solid Films*, 1996, **274**(1), p 106-112
12. S. Jain, A. Harker, A. Atkinson, and K. Pinardi, Edge-induced Stress and Strain in Stripe Films and Substrates: A Two-dimensional Finite Element Calculation, *J. Appl. Phys.*, 1995, **78**(3), p 1630-1637
13. S.M. Hu, Film-Edge-Induced Stress in Silicon Substrates, *Appl. Phys. Lett.*, 1978, **32**(1), p 5-7
14. S.M. Hu, Film-Edge-Induced Stress in Substrates, *J. Appl. Phys.*, 1979, **50**(7), p 4661-4666
15. S.C. Jain, H.E. Maes, K. Pinardi, and I. DeWolf, Stresses and Strains in Lattice-Mismatched Stripes, Quantum Wires, Quantum Dots, and Substrates in Si Technology, *J. Appl. Phys.*, 1996, **79**(11), p 8145-8165
16. X.C. Zhang, B.S. Xu, H.D. Wang, and Y.X. Wu, Analytical Modeling of Edge Effects on the Residual Stresses Within the Film/substrate Systems. I. Interfacial Stresses, *J. Appl. Phys.*, 2006, **100**(11), p 113525
17. E. Suhir, Stresses in Bi-Metal Thermostats, *J. Appl. Mech.*, 1986, **53**(3), p 657-660
18. E. Suhir, Interfacial Stresses in Bimetal Thermostats, *J. Appl. Mech.*, 1989, **56**(3), p 595-600
19. E. Suhir, An Approximate Analysis of Stresses in Multilayered Elastic Thin Films, *J. Appl. Mech.*, 1988, **55**(1), p 143-148
20. H. Yin, G. Paulino, and W. Buttlar, An Explicit Elastic Solution for A Brittle Film with Periodic Cracks, *Int J Fracture*, 2008, **153**(1), p 39-52
21. H. Yin, Opening-Mode Cracking in Asphalt Pavements Crack Initiation and Saturation, *Road Mater Pavement*, 2010, **11**(2), p 435-457
22. Z.C. Xia and J.W. Hutchinson, Crack Patterns in Thin Films, *J. Mech. Phys. Solids*, 2000, **48**(6-7), p 1107-1131
23. Z. Suo and J.W. Hutchinson, Interface Crack Between Two Elastic Layers, *Int J Fracture*, 1990, **43**(1), p 1-18
24. Z. Suo and J.W. Hutchinson, Steady-state Cracking in Brittle Substrates Beneath Adherent Films, *Int. J. Solids Struct.*, 1989, **25**(11), p 1337-1353
25. A. Bagchi and A.G. Evans, The Mechanics and Physics of Thin Film Decohesion and Its Measurement, *Interface Sci.*, 1996, **3**(3), p 169-193
26. J.L. Beuth, Cracking of Thin Bonded Films in Residual Tension, *Int. J. Solids Struct.*, 1992, **29**(13), p 1657-1675
27. J.P. Parmigiani and M.D. Thouless, The roles of toughness and cohesive strength on crack deflection at interfaces, *J. Mech. Phys. Solids*, 2006, **54**(2), p 266-287
28. J.W. Hutchinson and Z. Suo, Mixed-Mode Cracking in Layered Materials, *Adv. Appl. Mech.*, 1992, **29**, p 63-191